

SUPPORTING INFORMATION

Ring Closing Reaction in Diarylethene Captured by Femtosecond Electron Crystallography

Hubert Jean-Ruel^{1,2}, Meng Gao^{1,2}, Michal A. Kochman³, Cheng Lu¹, Lai Chung Liu^{1,2}, Ryan R. Cooney¹,
Carole A. Morrison³, and R.J.D. Miller^{*1,2}

- 1) Departments of Chemistry and Physics, University of Toronto, 80 St. George Street, Toronto, Ontario M5S 3H6, Canada
- 2) Max Planck Institute for the Structure and Dynamics of Matter, Luruper Chaussee 149, Hamburg 22761, Germany
- 3) School of Chemistry and EaStCHEM Research School, University of Edinburgh, The King's Buildings, West Mains Road, Edinburgh EH9 3JJ, United Kingdom

***dwayne.miller@mpsd.cfel.de**

Contents

1. Additional information on the data acquisition and averaging	3
2. Orientation determination	3
3. Theoretical t_{∞} differential images and Pearson correlation analysis	4
4. Model analysis	6
5. Calculation of the ground state structures	8
6. Calculation of the excited state open-ring intermediate structure.....	10
References	13

1. Additional information on the data acquisition and averaging

Since the thermal irreversibility of diarylethene limits the acquisition of *during* images to only one probe pulse at a time, single pulses were also used for the *before* and *after* images for adequate referencing when performing the time-resolved measurements (however, to increase the SNR, four *before* images were acquired for each pump-probe event). For purely static electron diffraction measurements, the *during* image was not acquired and 100 probe pulses (at 10 Hz) were accumulated for the *before* and *after* images at each cycle.

Although the t_{∞} measurements were also taken systematically during the time-resolved scans, the images presented in Figure 1a-f were obtained from purely static electron diffraction measurements. Every image corresponds to the average of 5 to 10 crystals from each of which approximately the first 10 ring closing and opening cycles are averaged.

For the FED experiment, as explained in the methods section, t_0 was determined from an entirely independent measurement¹ repeated regularly throughout the scans and for every sample. Then, to further optimize the quality of the t_0 determination and the combination of the scans together (mainly to compensate for possible sample holder tilt which may affect the t_0 determination), we used a maximum rephasing of 0.5 ps within the different samples and an additional maximum overall shift of 0.5 ps for the average time traces, based on the start of the time-resolved signals

2. Orientation determination

Since the different orientations were obtained by microtoming single crystals along different planes, the samples from each set were very uniform. For each set, one sample was selected for the orientation analysis. The different orientations were determined with the help of a simulation program developed in-house and reported previously²; it is capable of simulating the electron diffraction patterns for any orientation and explicitly considers the combined effect of electron beam divergence and mosaicity. It uses the kinematic theory for electron diffraction. The reference structure used for the simulation was obtained by X-ray diffraction and reported previously³.

First, a static diffraction pattern of the crystal in the open-ring state is obtained. After removing the diffuse electron scattering background from the experimental image, the position and relative intensity of the peaks observed are determined. They are then systematically compared to the positions and relative intensities simulated for the complete range of possible orientations (4π sr). The optimal orientation is the one for which the peak positions match and the R factor is minimal:

$$R = \frac{\sum |\sqrt{I_{sim}} - \sqrt{I_{obs}}|}{\sum \sqrt{I_{obs}}} \quad (S1)$$

where I_{obs} and I_{sim} are respectively the observed and simulated intensities. An example of image processing is shown in Figure S1 and the corresponding orientation match is shown in Figure S2.

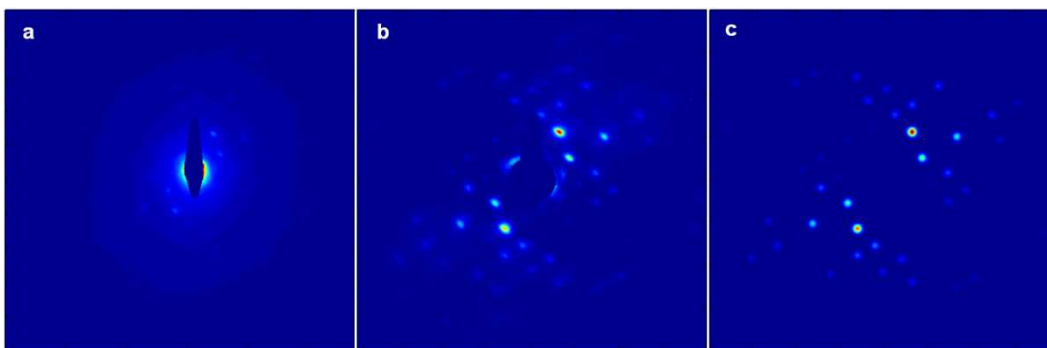


Fig. S1. Image processing for orientation determination. (a) Original image acquired. (b) Centered and background subtracted image. (c) Extracted intensities and positions.

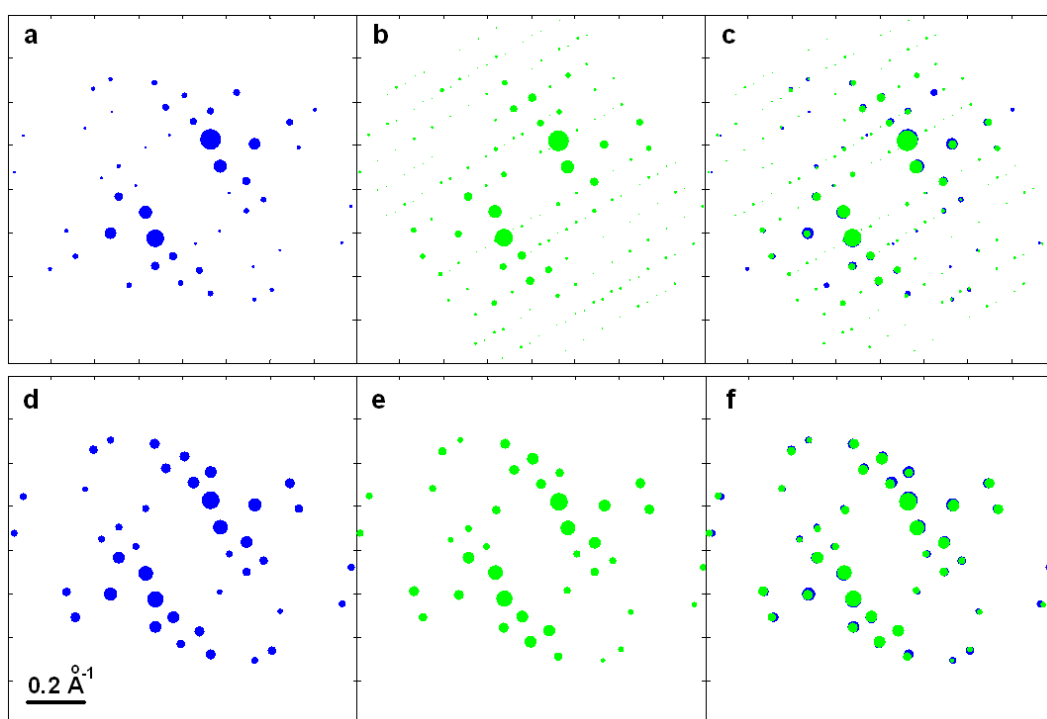


Fig. S2. Orientation matching. (a) Experimental extracted intensities and positions. (b) Simulated intensities and positions for the orientation $[uvw]=[0.45 \ 0.19 \ 0.87]$ ($[uvw]$ represents the fractional coordinates of the incident beam wave vector relative to the unit cell axes). (c) Experimental and simulated peaks overlaid. The spot areas are proportional to the diffraction intensity. The R value is 0.23. (d-f) Same as (a-c) but the spot areas are proportional to the structure factor amplitudes and only the matching peaks are shown.

3. Theoretical t_{∞} differential images and Pearson correlation analysis

The set of structure factors associated with the open- and the closed-ring optimized structures (see section 5 of the present document) were calculated using the kinematic theory for electron diffraction. The diffraction patterns associated with the open-ring state were obtained directly from the first set, using the simulation program mentioned above. As mentioned previously, only a fraction of the molecules undergo

ring closing during each cycle. In order to simulate the diffraction pattern of the closed-ring form, the two sets of structure factors were combined together according to a simple method presented previously for time-resolved crystallography analysis⁴. From the amplitude of the relative intensity changes, the fraction excited was estimated to be 2.9% by using a least square criterion and by considering 22 reliable high intensity peaks (more specifically by considering the 11 Friedel pairs for which at least one of the two peaks has an experimental open-ring intensity above 35% of the maximum intensity; a 12th pair fulfills this requirement but was rejected because the simulated open-ring intensity reproduces very poorly the experimental intensity, resulting in an unrealistically large simulated relative intensity change). To provide a more accurate comparison with the experimental data, relative rather than absolute simulated intensity changes – applied to the experimental open-ring intensities – were considered for the main peaks in the theoretical differential images (the main peaks being those for which the intensity is at least 15% of the maximum for both the experimental and simulated intensities). The comparison with the differential images obtained directly from considering the absolute simulated intensity changes is presented in Figure S3, showing that the difference is minimal.

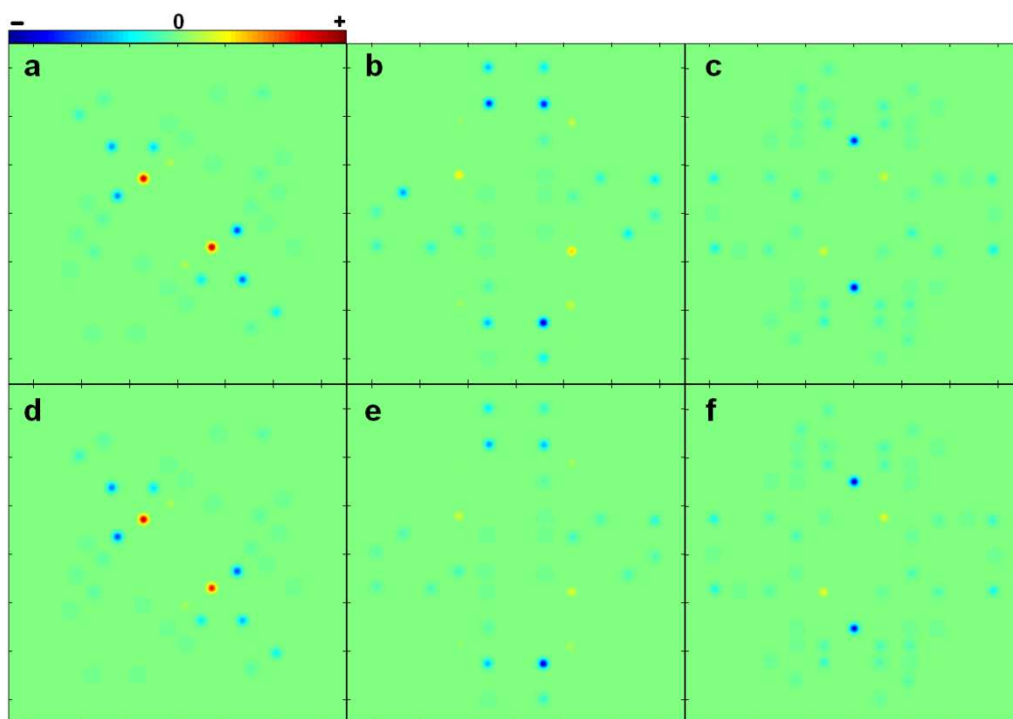


Fig. S3. Theoretical differential images. (a-c) Images obtained considering the absolute simulated intensity changes. (d-f) Corresponding images obtained considering the relative intensity changes applied to the experimental open-ring intensities for the strong peaks.

For the Pearson correlation coefficient calculation of the t_{∞} time point, the same 22 peaks were considered. This can be done either by using the relative intensity changes directly or applying them to the experimental open-ring intensities. Both methods yielded the same correlation value of 0.87.

For the Pearson correlation coefficient calculation of the average UED signal for the time points comprised between 10 and 50 ps, 4 of the 22 peaks were excluded because of the clear presence of strain signal. Using the relative intensity changes directly or applying them to the experimental open-ring intensities yielded correlation values of 0.92 and 0.94 respectively.

The Pearson correlation coefficient between two sets of intensity change ΔI_{exp} (experimental) and ΔI_{sim} (simulated) is given by:

$$r(\Delta I_{exp}, \Delta I_{sim}) = \frac{\sum_k C_{exp}(k) C_{sim}(k)}{\sqrt{\sum_k C_{exp}(k)^2} \sqrt{\sum_k C_{sim}(k)^2}} \quad (S2)$$

$$C_i(k) = \frac{\Delta I_i(k) - \overline{\Delta I_i}}{\overline{\Delta I_i}}$$

4. Model analysis

4.1 Model

In order to generate a pool of reasonable molecular structures to analyze the UED data, a model was constructed for the ring-closing reaction. We looked for the simplest set of basic motions that could convert the open-ring geometry into the closed-ring one. We found by inspection that three pairs of pure rotations and one pair composed of a pure rotation and a torsion could achieve this. Those four motions are shown in Figure S4. Figure S5 shows that their application to the open-ring geometry does result into the closed-ring one.

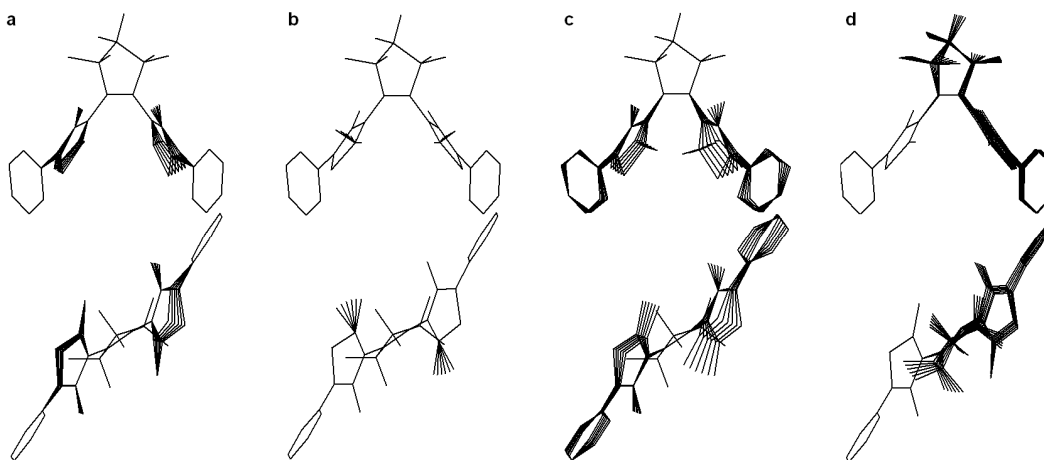


Fig. S4. The four motions which convert the open-ring geometry into the closed-ring one are shown. In each case 0%, 20%, 40%, 60%, 80%, and 100% of the final rotation required for the full conversion are shown. The hydrogen atoms and corresponding bonds are not included for clarity.

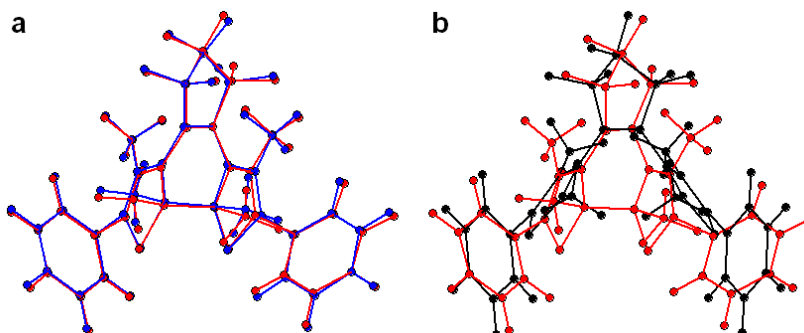


Fig. S5. (a) Model closed-ring structure (red) generated by the application of the four motions shown in Figure S4 to the calculated open-ring structure overlaid on the calculated closed-ring structure (blue). It should be noted that for two of the four motions, the hydrogen atoms were also slightly rotated separately from the main rotation. (b) For comparison: model closed-ring structure (red) overlaid on the calculated open-ring structure (black).

The four motions of the model were allowed to vary independently for a range going from -50% to 150% of the full rotations producing the ring-closed geometry (in steps of 10%), generating a large pool of molecular structures. To illustrate the large range of structures generated, two extreme cases are presented in Figure S6a-b, corresponding to the geometries obtained by setting all the motions to -50% or to 150% respectively.

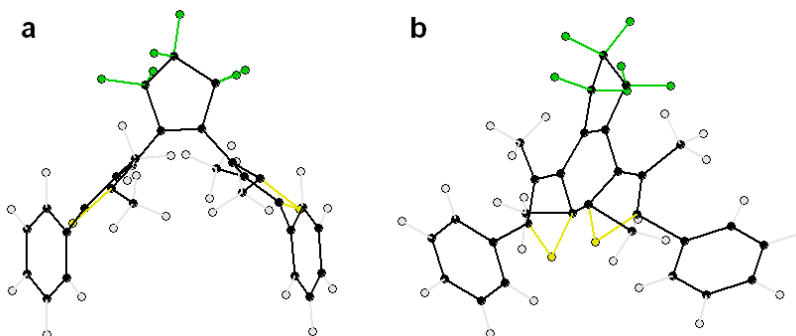


Fig.S6. (a) All motions set to -50%. (b) All motions set to 150%.

The set of structure factors associated with each model geometry was then calculated, from which the simulated relative diffraction intensity difference between the model and calculated open-ring structures were determined. Again, the fraction converted was estimated from the magnitude of the relative intensity changes at t_0 using a least square criterion and considering 22 peaks. It was found to be approximately 2.5%, slightly lower than what was obtained for the images presented in Figure 1 (and mentioned above in section 3). The reason is that in the latter case, only the first few cycles were averaged together. Here, 100 to 500 cycles per sample are averaged together and thus the optical fatigue⁵ reduces the average fraction converted (see inset of Figure 1d).

The simulated relative differences were then applied to the experimental open-ring intensities to provide a more accurate comparison with the experimental data.

4.2 Convergence of the time-resolved data towards a closed-ring structure

The average time-resolved diffraction intensity changes for the time delays between 10 and 50 ps were compared to the ones generated by the model structures (again considering 18 of the 22 peaks, i.e. the strongest reflections that do not exhibit strain wave signal). The method of least squares was used. The average of the top 1% best matching structures is presented in Figure S7 (which is the same as Figure 3a), along with the average of the top 1% best matching structures for time delays before $t=0$ for comparison. The convergence of the UED data towards a closed-ring structure qualitatively similar to the calculated one (Figure 1h) is obtained. The only significant difference is the position of the two methyl groups attached to the reactive carbon atoms, whose rotation did not converge appropriately likely in great part because of their limited effect on the diffraction patterns.

It is important to emphasize that this analysis is not meant to provide quantitative information, because of the limited diffraction data coverage and SNR, and also because of the imperfect reproduction of the experimental diffraction patterns by the simulations; it is rather for confirmation of the convergence towards a closed-ring molecule.

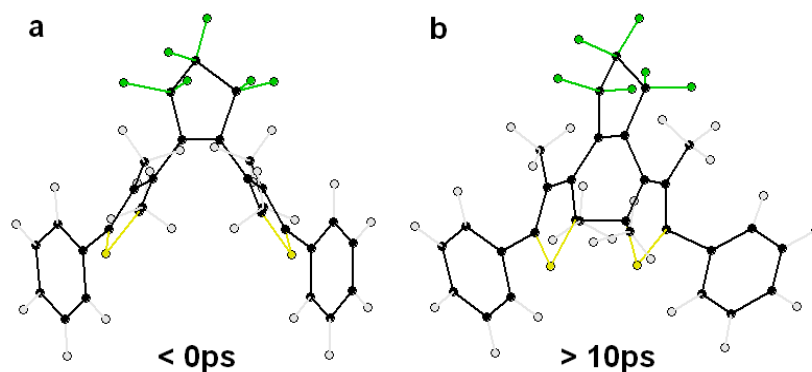


Fig. S7. Best matching model structure using the least squares method for the time delays (a) before $t=0$, and (b) between 10 and 50 ps. The top 1% matching structures were averaged together to obtain a representative result of the overall convergence.

4.3 Qualitative analysis of the time resolved data immediately following photoexcitation

The amount of reliable experimental data available to investigate the intermediate structure is further limited by its short lifetime and the lower SNR achieved. The level of noise – in particular for the low intensity peaks – prevents us from performing an accurate model convergence analysis similar to that presented above for the late time points. Nevertheless, we attempted to identify a possible trend with respect to the thiophene and perfluorocyclopentene rotations. It is apparent from Figure 2 that reflections (5 1 -6) and (2 0 -4) are particularly reliable and sensitive to the structural changes involved. They present both the strongest diffraction intensities and the largest time-resolved signals among the two orientations which were probed with short time steps (orientations of Figure 1b-c). We also considered the next seven strongest peaks (those above 65% of maximum intensity), which did not exhibit signal above noise but still participated to further constrain the fit. Again, the method of least squares was used to obtain the histogram shown in Figure 3. The result suggests that the formation of the intermediate structure involves a large rotation of the thiophene rings while the perfluorocyclopentene moiety is only slightly rotated. Although this simple analysis cannot provide quantitative information on the intermediate structure – in particular the degree of rotation of the thiophene ring is certainly overestimated – the general noted behaviour is reasonable. It is interesting to point out that a qualitatively similar result is obtained by considering only the two key reflections (5 1 -6) and (2 0 -4).

5. Calculation of the ground state structures

5.1. Computational methods

The density functional theory calculations that were performed in order to optimize the geometries of the open- and closed-ring forms (labelled HT and CHD respectively) embedded in the open-ring crystal lattice are now discussed in detail. As mentioned previously, in this experiment, only a small fraction of the molecules in the crystal underwent ring closing during each cycle and the converted molecules were distributed randomly and uniformly in the irradiated solid. Hence, an appropriate theoretical model for the crystal after irradiation is a single reactive molecule embedded in the bulk lattice consisting of nonreactive molecules. Because of computational demands, in all calculations a single unit cell (one reactive and three nonreactive molecules, with 236 atoms in total) was used. As the four molecules

contained in the unit cell are related by symmetry, and therefore start off as equivalent, it does not matter which molecule is selected as the reactive one. In what follows, CHD@crystal refers to a model where one CHD molecule is embedded in a crystallographic unit cell along with three nonreactive (HT) molecules. Similarly, HT@crystal refers to a model where all four molecules are in the HT state.

For these geometry optimizations, the generalized gradient approximation by Perdew, Burke, Ernzerhof⁶ (PBE) was utilized, as implemented in the software package CASTEP version 5.0.⁷ The electronic Brillouin zone was sampled using a Monkhorst-Pack k -point grid with a k -point spacing of at most 0.05 \AA^{-1} , resulting in a total of three k -points. A plane-wave cutoff of 500 eV was used, which was demonstrated to converge the total electronic energy to within 2 meV/atom, along with the default ultrasoft pseudopotentials as included in the CASTEP package⁸. Energies and forces were corrected for dispersion interactions using the semi-empirical scheme of Grimme⁹.

Geometries were optimized using the default BFGS algorithm using the experimental crystal structure³ as the starting point, with fixed cell dimensions ($a = 24.023 \text{ \AA}$, $b = 8.466 \text{ \AA}$, $c = 13.350 \text{ \AA}$, $\alpha = \gamma = 90^\circ$, $\beta = 109.24^\circ$). The default geometry convergence criteria were applied (energy tolerance: $2 \times 10^{-5} \text{ eV/atom}$, maximum force tolerance: 0.05 eV \AA^{-1} , and maximum displacement tolerance: 0.001 \AA).

5.2. Results

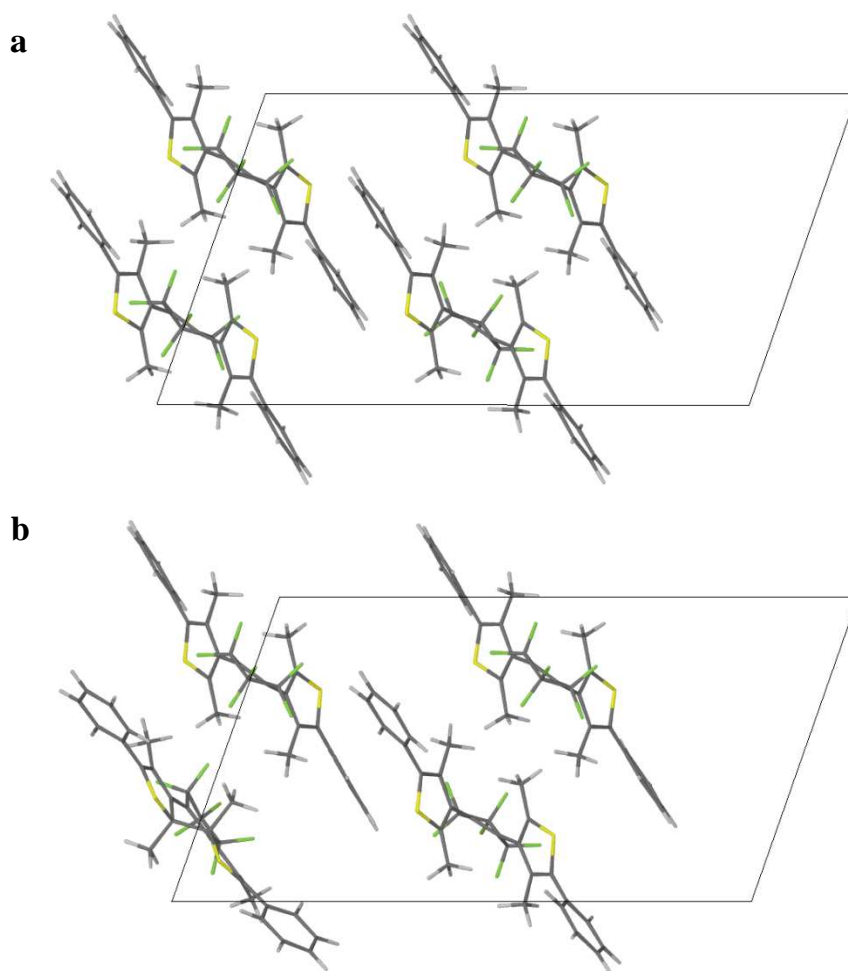


Fig. S8. Structures of (a) HT@crystal and (b) CHD@crystal optimized at the DFT level of theory.

The resulting minimum geometries of HT@crystal and CHD@crystal are shown in Figure S8a-b, respectively. In HT@crystal, the distance between the reactive carbon atoms is 3.712 Å, whereas in the converted molecule of CHD@crystal, it is 1.566 Å, which is typical of bonds between sp^3 -hybridized carbons. It can also be observed that the cyclization is accompanied by a displacement of the two phenyl rings of the reactive molecule from their original positions. The effect of the ring-closing is found to be minimal on the surrounding molecules.

6. Calculation of the excited state open-ring intermediate structure

The calculations that were performed in order to optimize the geometry of the open-ring intermediate structure embedded in the open-ring crystal lattice (referred to in what follows as HT*@crystal) are now discussed in detail. Since this structure is formed through electronic excitation of the crystal, the potential energy surface for the optimization of HT*@crystal cannot be generated using only the ground-state DFT method. Due to the relative weakness of intermolecular interactions that is characteristic of molecular crystals in the absence of localized interactions such as hydrogen bonding and π -stacking, it is justified to make the approximation that the electronic excitation is localized on the reactive molecule and that all other molecules exist in the electronic ground state. This approximation paved the way for treating the reactive molecule using an electronic structure method capable of describing excited electronic states while continuing to use ground-state DFT to describe the surrounding nonreactive molecules.

6.1. Computational methods

A detailed description of the subtractive QM/QM hybrid method that was used to combine the description of the photoexcited molecule and the surrounding bulk lattice using two distinct quantum mechanical methods is presented elsewhere^{10,11}. Only the simulation parameters specific to the geometry optimization of HT*@crystal are presented here.

The reactive molecule was described using the complete active space SCF (CASSCF) method with a localized basis set while the nonreactive molecules which represent the bulk lattice were treated using DFT with a plane-wave basis set. The total energy of the simulated system was given by the following equation:

$$\frac{E_{\text{CASSCF}}}{\text{DFT}}(S) = E_{\text{DFT}}^{\text{PW}}(S) + E_{\text{CASSCF}}^{\text{GTO}}(C + L) - E_{\text{DFT}}^{\text{GTO}}(C + L) \quad (\text{S3})$$

The subscripts DFT and CASSCF refer to the electronic structure method used, while the superscripts PW (plane wave) and GTO (Gaussian-type orbital) refer to the basis sets used for the evaluation of the respective terms. The partitioning of the system into CASSCF and DFT regions is shown schematically in Figure S9 below. S denotes the entire system, C the reaction site and L the link atoms introduced to cap covalent bonds cut by the CASSCF/DFT boundary. As will be explained below, only the fragment of the reactive molecule that is directly involved in the cyclization reaction was considered part of the reaction site C . Covalent bonds cut by the boundary between the reaction site C and the rest of the system were capped by a number of link atoms L (not shown in Figure S9). The union of the reaction site C and the link atoms L is considered the CASSCF region, and the remainder of the system is termed the DFT region.

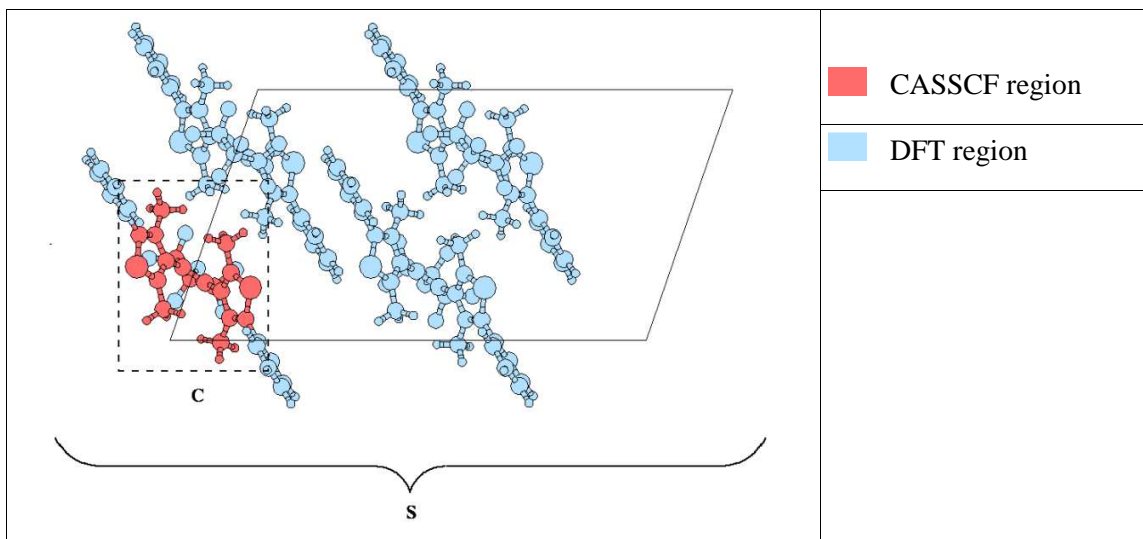


Fig. S9. Partitioning of the system into CASSCF and DFT regions.

The term $E_{DFT}^{PW}(S)$ was evaluated through a periodic DFT calculation, and it includes all interactions between the reactive molecule and the surrounding molecules. $E_{CASSCF}^{GTO}(C + L)$ and $E_{DFT}^{GTO}(C + L)$ are the intramolecular energies of the reactive molecule, with link atoms, calculated respectively at the CASSCF and DFT levels in the absence of the surrounding periodic lattice. $E_{CASSCF}^{GTO}(C + L)$ was calculated using a localized (Gaussian-type orbital) basis set. $E_{DFT}^{GTO}(C + L)$ was subtracted from $E_{DFT}^{PW}(S) + E_{CASSCF}^{GTO}(C + L)$ in order to correct for the double counting of interactions within the CASSCF region by the first and second terms on the right-hand-side of equation 1. This term may, in principle, be calculated using either a localized or plane-wave basis set. In practice, a plane-wave DFT calculation on a large isolated molecule would require a large simulation cell due to the need to surround the molecule with a layer of vacuum, and it is far cheaper to calculate $E_{DFT}(C + L)$ using a localized basis set. This is equivalent to introducing an additional error into the calculation, whereby the cancellation of intramolecular forces between $E_{DFT}^{PW}(S)$ and $E_{DFT}^{GTO}(C + L)$ is inexact. Nonetheless, given the other sources of error inherent in the subtractive QM/QM scheme, calculating $E_{DFT}(C + L)$ using a localized basis set is justified.

The diarylethene molecule is too large to be treated in its entirety using the CASSCF method. Therefore, the two phenyl groups and six fluorine atoms were excluded from the CASSCF calculation, and the resulting eight dangling bonds were capped by hydrogen link atoms. As in a standard QM/MM calculation, the purpose of the link atoms in the QM/QM calculation is to saturate covalent bonds cut by the boundary between the CASSCF and DFT regions. The link atoms were included in the $E_{CASSCF}^{GTO}(C + L)$ and $E_{DFT}^{GTO}(C + L)$, but excluded from the term $E_{DFT}^{PW}(S)$.

Since the link atoms are not part of the real physical system, but rather *ad hoc* constructs intended to prevent artifacts at the boundary, they must be positioned in such a way as to avoid introducing unphysical degrees of freedom into the simulation. The link atom positioning scheme adopted in the present simulation is as follows. Let j and k represent an atom in the CASSCF region and an atom in the DFT region, respectively, and they are connected to each other by a covalent bond. The link atom l for that bond is positioned at a fixed fraction s of the j - k distance, such that:

$$\mathbf{R}_l = s\mathbf{R}_k + (1 - s)\mathbf{R}_j \quad (\text{S4})$$

Thus, the position of the link atom is determined completely by the positions of the real atoms j and k , and its existence does not introduce unphysical degrees of freedom into the system. The fraction s is chosen such as to reflect the ratio between j - l and j - k equilibrium bond lengths. For the C-C(phenyl) bonds cut by the CASSCF/DFT boundary, s was set to 0.744 according to the ratio between Ph-H and Ph-CH₂CH₃ bond lengths, as determined by calculations at the PBE/6-31G(d) level of theory. Similarly, for the C-F bonds cut by the boundary, s was set to 0.808, reflecting the ratio of the C-H bond length in ethane and the C-F bond length in *anti*-1,1,2,2-tetrafluoroethane, determined by calculations at the same level of theory as reported above.

Although the link atoms are not part of the real system, forces do exist on them, originating from the terms $E_{\text{CASSCF}}^{\text{GTO}}(C + L)$ and $E_{\text{DFT}}^{\text{GTO}}(C + L)$. In the link atom placement scheme defined by equation (S4), the force acting on a link atom l is redistributed on the atoms j and k according to:

$$\begin{aligned}\mathbf{F}'_j &= \mathbf{F}_j + (1 - s)\mathbf{F}_l \\ \mathbf{F}'_k &= \mathbf{F}_k + s\mathbf{F}_l\end{aligned}\quad (\text{S5})$$

It is trivial to verify that this redistribution of forces preserves both the net force and the total torque on the atoms j , k and l .

The term $E_{\text{DFT}}^{\text{PW}}(S)$ was evaluated using the Perdew, Burke, Ernzerhof exchange-correlation functional⁶ as implemented in the software package CASTEP version 5.0⁷. A plane-wave cutoff of 400 eV was applied, which was demonstrated to converge the total energy to within 5 meV/atom. The electronic Brillouin zone was sampled at the (0, 1/4, 0)-point only. The default ultrasoft pseudopotentials were used⁸; energies and forces were corrected for dispersion interactions using the semiempirical scheme of Grimme⁹.

The term $E_{\text{CASSCF}}^{\text{GTO}}(C + L)$ was evaluated using the CASSCF method as implemented in the computational chemistry program Gaussian 09¹². The CASSCF calculations employed an active space consisting of 10 electrons in 10 π and π^* orbitals. As a compromise between computational cost and feasibility, the 3-21G basis set was employed in the CASSCF calculations. Exploratory geometry optimizations of the CASSCF region **C+L** in isolation from the surrounding lattice showed that equilibrium HT* structures obtained using the 6-31G and 3-21G basis sets are in reasonably good agreement. Of particular concern is the distance between the reactive carbons; the 3-21G basis set was found to underestimate this distance by 0.18 Å, which was deemed acceptable for the purposes of the present study. Finally, the term $E_{\text{CASSCF}}^{\text{GTO}}(C + L)$ was calculated using the Gaussian 09 implementation of the PBE functional using the 6-31G(d) basis set.

The geometry of the entire system (S) was optimized using the gradient descent algorithm in Cartesian coordinates to a maximum force tolerance of 0.025 eV/Å and root mean square force tolerance of 0.01 eV/Å.

6.2. Results

The equilibrium structure of HT*@crystal, overlaid on that of HT@crystal, is presented in Figure S10. The main geometry difference between HT*@crystal and HT@crystal is the position of the thiophene rings of the reactive molecule, with these rings becoming near-coplanar in HT*@crystal, and the distance between the reactive carbons shortening to 2.188 Å. The positions of the phenyl rings of the reactive molecule differ only slightly between HT@crystal and HT*@crystal. Likewise, there is little structural rearrangement in the nonreactive molecules, with the greatest structural change being slight rotations (around 10°) around the axis of their fluorinated cyclopentene ring. In absolute terms, however, these structural changes are slight.

The fact that HT* appears as an energy minimum on the potential energy surface of the photoexcited molecule embedded in the crystal lattice suggests that the reaction mechanism predicted theoretically¹³ for the isolated molecule persists in the solid. Furthermore, the small magnitude of structural rearrangement in the surrounding DFT molecules is consistent with the experimental finding that the photocyclization reaction is fully reversible.

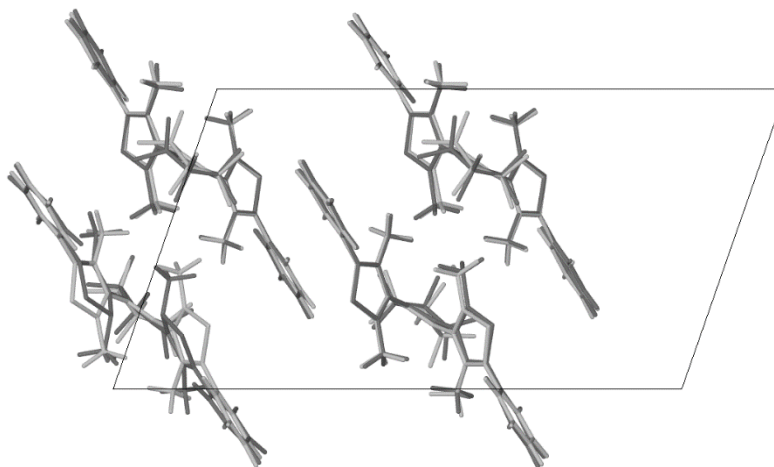


Fig. S10. Overlaid structures of HT*@crystal (dark grey) and HT@crystal (light grey).

References

- 1 Dwyer, J. R. *et al.* Femtosecond Electron Diffraction: 'Making the Molecular Movie'. *Philosophical transactions. Series A, Mathematical, physical, and engineering sciences* **364**, 741-778 (2006).
- 2 Gao, M. *et al.* Mapping molecular motions leading to charge delocalization with ultrabright electrons. *Nature* **496**, 343-346 (2013).
- 3 Irie, M., Kobatake, S. & Horichi, M. Reversible surface morphology changes of a photochromic diarylethene single crystal by photoirradiation. *Science* **291**, 1769-1772 (2001).
- 4 Coppens, P., Vorontsov, I., Graber, T., Gembicky, M. & Kovalevsky, A. Y. The structure of short-lived excited states of molecular complexes by time-resolved X-ray diffraction. *Acta crystallographica. Section A, Foundations of crystallography* **61**, 162-172 (2005).
- 5 Irie, M. Diarylethenes for Memories and Switches. *Chemical reviews* **100**, 1685-1716 (2000).
- 6 Perdew, J. P., Burke, K. & Ernzerhof, M. Generalized Gradient Approximation Made Simple. *Physical review letters* **77**, 3865-3868 (1996).
- 7 Clark, S. J. *et al.* First principles methods using CASTEP. *Zeitschrift für Kristallographie - Crystalline Materials* **220**, 567-570 (2005).
- 8 *Materials Studio CASTEP Online Help.* H_00PBE.usp uses one valence electron (s state), C_00PBE.usp uses four valence electrons (s and p state), and N_00PBE.usp uses five valence electrons (s and p state).
- 9 Grimme, S. Semiempirical GGA-type density functional constructed with a long-range dispersion correction. *Journal of computational chemistry* **27**, 1787-1799 (2006).

- 10 Senn, H. & Thiel, W. in *Atomistic Approaches in Modern Biology* Vol. 268 *Topics in Current Chemistry* (ed Markus Reiher) Ch. 84, 173-290 (Springer Berlin Heidelberg, 2007).
- 11 Kochman, M. A., Bil, A. & Morrison, C. A. Hybrid QM/QM simulations of photochemical reactions in the molecular crystal N-salicylidene-2-chloroaniline. *Physical Chemistry Chemical Physics* **15**, 10803-10816 (2013).
- 12 Frisch, M. J. *et al.* *Gaussian 09, Revision B.01* (2009).
- 13 Boggio-Pasqua, M., Ravaglia, M., Bearpark, M. J., Garavelli, M. & Robb, M. A. Can Diarylethene Photochromism Be Explained by a Reaction Path Alone? A CASSCF Study with Model MMVB Dynamics. *The Journal of Physical Chemistry A* **107**, 11139-11152 (2003).